PHYSICAL REVIEW B **93**, 085423 (2016)

Amorphous to crystalline phase transition: Onset of pattern formation during ion erosion of Si(001)

Martin Engler[1,2,*] and Thomas Michely[1,†]

[1]*II. Physikalisches Institut, Universität zu Köln, Zülpicher Straße 77, 50937 Köln, Germany*

[2]*Helmholtz-Zentrum Dresden-Rossendorf, Institute of Ion Beam Physics and Materials Research, Bautzner Landstraße 400, 01328 Dresden, Germany*

(Received 30 October 2015; revised manuscript received 26 January 2016; published 16 February 2016)

The morphological evolution of Si(001) is investigated for normal incidence 2 keV Kr^+ ion irradiation under ultra-high vacuum conditions as a function of temperature and ion fluence through scanning tunneling microscopy and low energy electron diffraction. Under the conditions chosen, the selvage of Si(001) amorphizes below the critical temperature T_c of 670 K, while above it remains crystalline. Below T_c the sample remains flat, irrespective of the ion fluence. Above T_c, the crystalline sample displays for fixed ion fluence and as a function of sample temperature a pronounced roughness maximum at 700 K. Around this temperature, with increasing ion fluence a strong increase of roughness as well as coarsening are observed. Pyramidal pits and mounds develop, with facets formed by Si steps and narrow reconstructed terraces. Most exciting, with increasing ion fluence the pattern reorients from pits and mounds with edges along the $\langle 110\rangle$ directions to ridges and valleys rotated $\approx 45^\circ$ to the $\langle 110\rangle$ directions.

DOI: 10.1103/PhysRevB.93.085423

I. INTRODUCTION

The promise of self-organized ion beam pattern formation [1,2] on surfaces is to yield cheap, large area, and uniform nanopatterns that are useful for applications, e.g., as templates [3,4] or for direct modification of, e. g., optical properties [5,6].

Intense research in the past focused on temperature dependent ion beam pattern formation on metals [7–14], materials that remain crystalline during ion irradiation, and room temperature pattern formation on elemental semiconductors [2,15–25], materials that amorphize under these conditions. While ion beam pattern formation on crystalline surfaces is described in terms of atomic processes [9,26,27], a continuum description is adequate for materials that ion beam amorphize [2,28].

Materials that ion beam amorphize at low temperatures and remain crystalline at high temperatures offer the unique possibility to directly see the strength of destabilization due to the onset of crystalline structure, without changing chemistry and collision kinetics. Up to now only few studies investigated pattern formation for a material over a temperature range including the amorphous to crystalline phase transition. Noteworthy are the early ion beam pattern formation studies studies of Chey *et al.* [29] for Ge(001) and of Ozaydin *et al.* [30]. Recently, Ou *et al.* [31] demonstrated that for ion irradiation of Ge(001) rather close with the temperature induced transition from ion beam amorphization of the selvage to a crystalline selvage, a transition from a flat surface to a well developed checkerboard pattern of mounds and pits takes place. Such patterns formed just above the critical temperature of crystallization T_c may be remarkably regular and are probably the most regular nanoscale ion beam patterns that were created [32].

Therefore the temperature induced transition from an ion beam amorphized sample below T_c to an ion beam pattern in a crystalline selvage above T_c is key to understand these new, highly regular patterns and deserves our scientific interest. Here we present a detailed morphological scanning tunneling microscopy (STM) study of Si(001) ion beam pattern formation, able to resolve atomic scale details, and performed in fine temperature steps over the amorphous to crystalline phase transition around T_c. We conduct our research under ultrahigh vacuum conditions, since the purity and state of the surface is of crucial importance for the reproducibility of pattern formation, when surface diffusion processes are decisive. We pay special attention to measure a precise surface temperature by calibration experiments and to monitor *in situ* the crystallinity of our samples after ion erosion. Simultaneously with the amorphous to crystalline transition at $T_c = 670$ K we find an extremely sharp onset of pattern formation. Pattern formation culminates only 30 K above T_c in a regular mound and pit pattern with a sample roughness more than an order of magnitude higher than at T_c. The temperature dependent mechanisms of pattern formation and decay are analyzed. Unexpectedly, fluence dependent experiments around the temperature of maximum pattern amplitude reveal a pattern transition on the mesoscopic scale, not observed before: The mound and pit pattern aligned initially along the $\langle 110\rangle$ directions transforms with increasing fluence to a pattern of short ridge and valley segments rotated close to the $\langle 001\rangle$ directions. We show that this pattern rotation is a direct consequence of pattern coarsening.

II. EXPERIMENT

The experiments were conducted in an ultrahigh vacuum system with a base pressure below 6×10^{-11} mbar. For 2 keV Kr^+ irradiation a differentially pumped, scanned fine focus ion source was used. The pressure remained below 2×10^{-8} mbar during ion irradiation. Before and after each experiment the ion flux was measured with a Faraday cup moved into the sample position. The sample was heated with an electron beam heater from the backside. We measured the sample temperature with a thermocouple, which is attached temporarily to the sample.

---

[*] m.engler@hzdr.de

[†] michely@ph2.uni-koeln.de

The thermocouple was calibrated by observing the melting of small lead and indium droplets on a silicon sample. The samples were cleaved from a commercial n-doped Si(001) wafer and mounted with a defined azimuthal orientation. Before each experiment, the sample was irradiated at room temperature by 2 keV Kr^+ under an angle of 30° with respect to the surface normal. Thereby, the native oxide was removed and a well defined initial sample state with an initial roughness below 0.3 nm was established. Before irradiation, the samples were kept at the irradiation temperature for 1800–3600 s until the required heating power had stabilized. During ion beam irradiation the thermocouple was detached from the surface to avoid sputtering of atoms from the thermocouple wire onto the sample. After irradiation, the temperature was checked again with the thermocouple. During the experiments, the temperature changed less than 10 K. Due to the low average ion fluxes $\Phi \leqslant 1.4 \times 10^{18}\,\mathrm{ions/(s\,m^2)}$ used, ion beam heating of the sample is negligible. The sample heating was switched off no later than 120 s after the end of irradiation. After switching off the heating, the sample is quenched in less than 30 s to <500 K. The samples were analyzed *in situ* with low energy electron diffraction (LEED) and STM.

For analyzing the STM images the software GWYDDION was used [33]. For height representation in the STM topographs, a color palette was applied that changes with increasing height from black via red, orange, and yellow to white. The surface roughness σ is characterized by the root-mean-square roughness. The structure width λ is determined from the peak position in the radially averaged power spectral density function. Roughness σ and structure width λ are averages obtained from $1.4\,\mu\mathrm{m} \times 1.4\,\mu\mathrm{m}$ STM topographs, each with 1024×1024 pixels, taken at different positions on the sample. To enhance the visibility of surface features on different terraces, the detail STM images, with at least 256×256 pixels, are represented as a superposition of the original topography and a Sobel filtered version of the same image. The slope angle distributions were calculated from unfiltered, background corrected $1.4\,\mu\mathrm{m} \times 1.4\,\mu\mathrm{m}$ STM topographs using a custom software routine described in Ref. [18].

III. TEMPERATURE DEPENDENCE

An overview on the temperature dependent morphological evolution upon ion erosion of Si(001) is given by two series of experiments represented in Figs. 1 and 2 for fixed ion fluence $F = 5 \times 10^{21}\,\mathrm{ions/m^2}$ as well as ion fluxes of $\Phi = 1.4 \times 10^{18}\,\mathrm{ions/(s\,m^2)}$ and $\Phi = 4.8 \times 10^{17}\,\mathrm{ions/(s\,m^2)}$, respectively. For each experiment, a $1.4\,\mu\mathrm{m} \times 1.4\,\mu\mathrm{m}$ STM topograph, a filtered detail image, with the LEED pattern as inset, and the slope angle distribution are shown. At 664 K

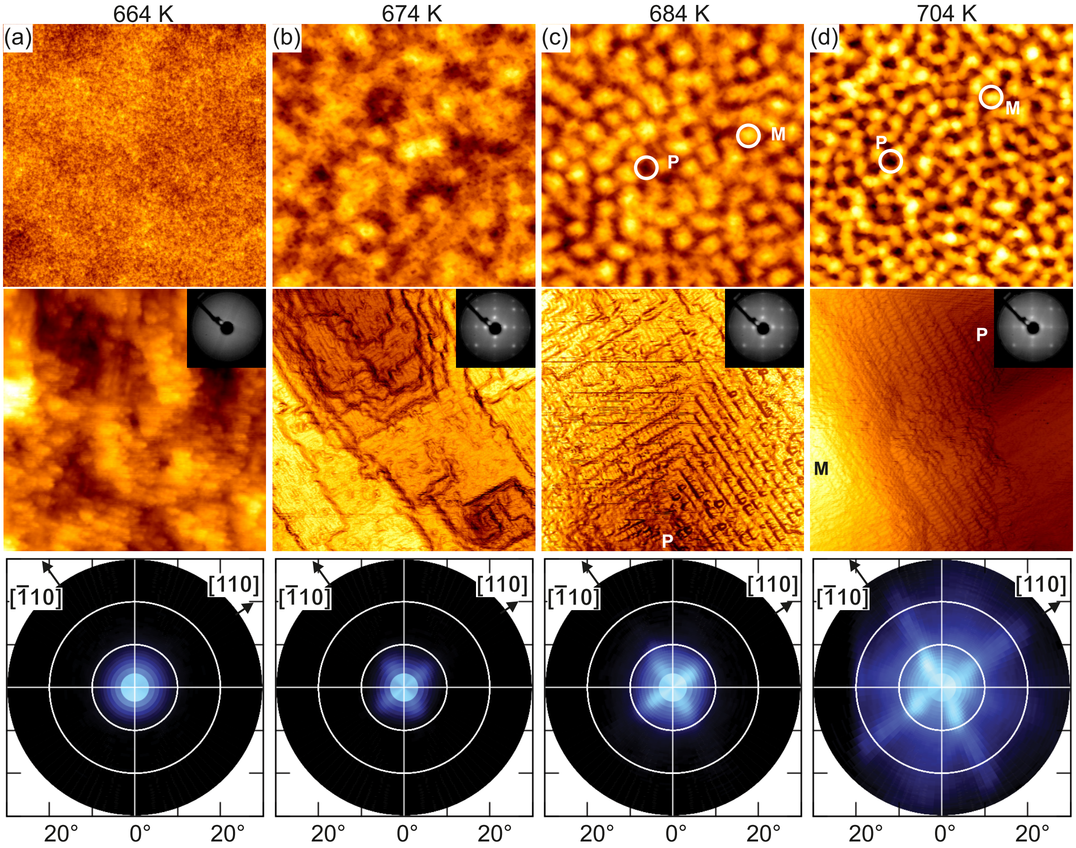

FIG. 1. Si(001) after 2 keV Kr^+ ion irradiation with $\Phi = 1.4 \times 10^{18}\,\mathrm{ions/(s\,m^2)}$ and $F = 5 \times 10^{21}\,\mathrm{ions/m^2}$. The temperatures are shown above each column. In the top row a $1.4\,\mu\mathrm{m} \times 1.4\,\mu\mathrm{m}$ STM topograph is shown. The z scales are (a) 2 nm, (b) 7 nm, (c) 11 nm, and (d) 16 nm. The middle row displays $45\,\mathrm{nm} \times 45\,\mathrm{nm}$ filtered detail images. The insets are LEED patterns at 66 eV electron energy. The bottom row displays the distribution of slope angles for the $1.4\,\mu\mathrm{m} \times 1.4\,\mu\mathrm{m}$ topographs. The directions indicated in the slope distributions apply also to the STM topographs. Some pits and mounds are labeled by letters P or M, respectively.

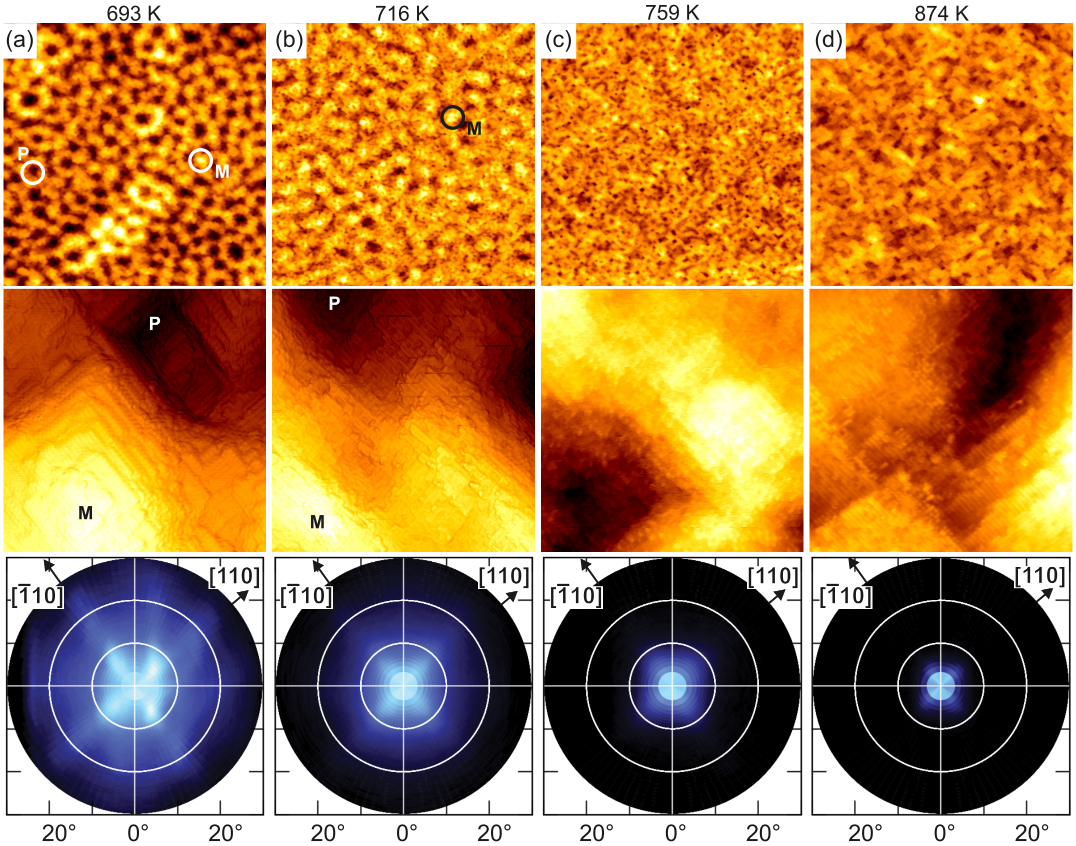

FIG. 2. Si(001) after 2 keV Kr$^+$ ion irradiation with $\Phi = 4.8 \times 10^{17}$ ions/(s m^2) and $F = 5 \times 10^{21}$ ions/m^2. The temperatures are shown above each column. In the top row a $1.4\,\mu$m $\times$ $1.4\,\mu$m STM topograph is shown. The z scales are (a) 17 nm, (b) 9 nm, (c) 4.5 nm, and (d) 3.7 nm. The middle row displays 45 nm $\times$ 45 nm filtered detail images with the same orientation as the overview images in the top row. The bottom row displays the distribution of slope angles for the $1.4\,\mu$m $\times$ $1.4\,\mu$m topographs. The directions indicated in the slope distributions apply also to the STM topographs. Some pits and mounds are labeled by letters *P* or *M*, respectively.

the surface is amorphous after ion irradiation, as obvious from the LEED pattern and the detailed image in Fig. 1(a). The surface is smooth with a roughness of $\sigma \approx 0.2$ nm. For ion exposure at 674 K and above, the surface remains crystalline. The LEED patterns show the characteristic spots of the Si(001) dimer row reconstruction. The dimer rows are visible in the detailed images of Figs. 1(b)–1(d) and 2(a). At 674 K small vacancy clusters can be seen on the terraces [see detailed image of Fig. 1(b)] indicating that at this temperature surface vacancy diffusion is still limited. Based on the observation of an amorphous sample at 664 K and a crystalline one at 674 K we set $T_c = 670$ K.

Between 684 and 716 K the surface morphology is dominated by pyramidal pits and mounds [Figs. 1(c) and 1(d) and 2(a) and 2(b)]. The facets of the pyramids are parallel to the $\langle 110 \rangle$ directions. They are composed of ≈2-nm-wide terraces and double steps perpendicular to the dimer rows, which is the equilibrium surface morphology of vicinal Si(001) with miscut angles larger than 6° [34,35]. These facets produce the spots in the slope distributions between 6° and 10° in the $\langle 110 \rangle$ directions. Around 700 K the steepest slopes in the $\langle 110 \rangle$ direction are 20°–25°, corresponding to $\{113\}$ facets. These are the slopes of the step bunches visible in Fig. 1(d). For temperatures above ≈750 K [Figs. 2(c) and 2(d)] pyramids are not more observed and only small pits are distributed over the surface. The pit width increases with temperature.

A quantitative analysis of the temperature dependent roughness evolution as shown in Fig. 3(a) displays a striking tenfold rise of roughness by increasing the temperature from $T_c = 670$ K to ≈700 K. At even higher temperatures, the surfaces roughness decreases again to $\sigma = 0.5$ nm at $T > 750$ K. The maximum in roughness at $T \approx 700$ K corresponds to a minimum in structure width λ [compare Fig. 3(b)].

IV. FLUENCE DEPENDENCE

For the temperature $T = (704 \pm 10)$ K of fastest roughening we investigated the surface morphology as a function of ion fluence at a constant flux of $\Phi = 1.4 \times 10^{18}$ ions/(s m^2). Each subfigure of Fig. 4 displays an overview STM image, two filtered detail STM images, and the corresponding slope distribution. The evolution of surface roughness σ and structure width λ is summarized in Fig. 5. It is obvious from Fig. 5(a) that the roughness increases monotonically with increasing fluence F. Similar, from Fig. 5(b) a strong coarsening of the structures with ion fluence can be inferred, though between $F = 1.5 \times 10^{20}$ ions/m^2 and $F = 7.5 \times 10^{20}$ ions/m^2 the structure width λ stagnates.

At $F = 3.0 \times 10^{19}$ ions/m^2, the surface morphology is dominated by a long wavelength background. On top of these long wavelength modulations, there are small rectangular pits and mounds with a depth/height of only 0.4–0.5 nm [Fig. 4(a)]

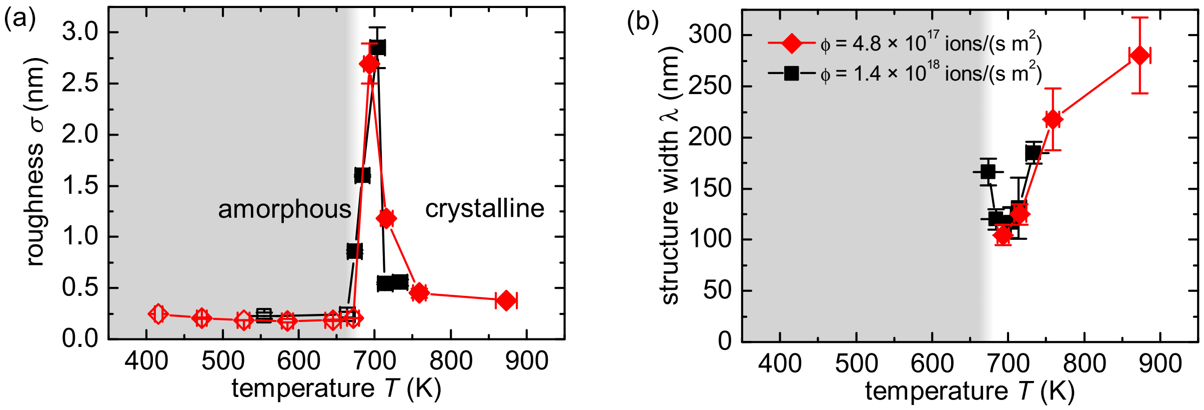

FIG. 3. Temperature dependence of (a) roughness σ and (b) structure width λ. Open symbols indicate amorphous and filled symbols crystalline surfaces.

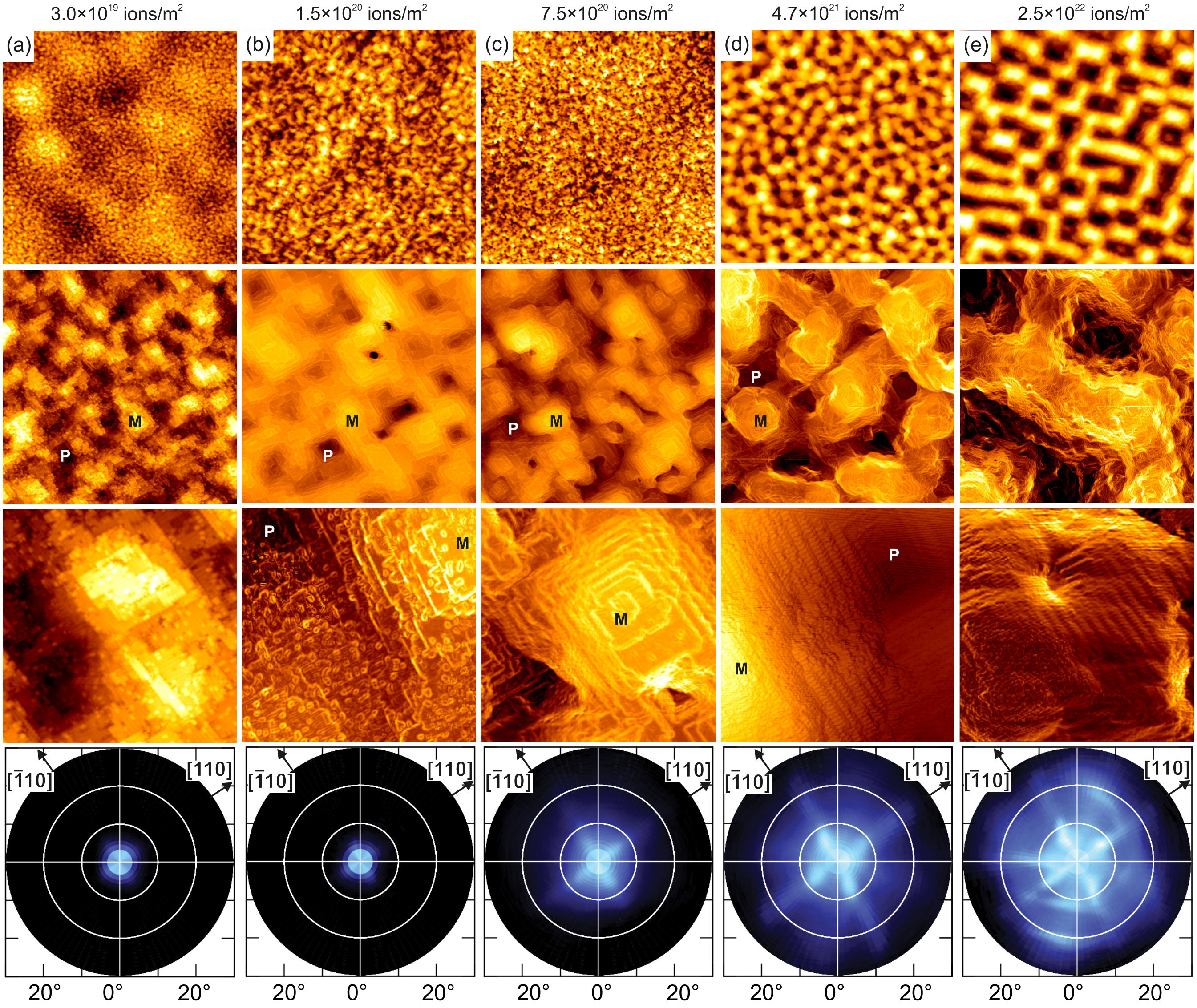

FIG. 4. Fluence dependence of surface morphology at $T = 704$ K. The fluence is shown above each column. In the top row 1.4 μm × 1.4 μm STM topographs are shown. The z scales are (a) 2.0 nm, (b) 2.3 nm, (c) 4.0 nm, (d) 16 nm, and (e) 24 nm. The crystallographic directions are indicated by arrows. The second and third rows display filtered images. In the second row, the image sizes are (a)–(c) 180 nm × 180 nm, and (d), (e) 360 nm × 360 nm. In the third row, their images sizes are 45 nm × 45 nm. The bottom row displays the distribution of slope angles for the 1.4 μm × 1.4 μm topographs. The directions indicated in the slope distributions apply also to the STM topographs. Some pits and mounds are labeled by letters P or M, respectively.

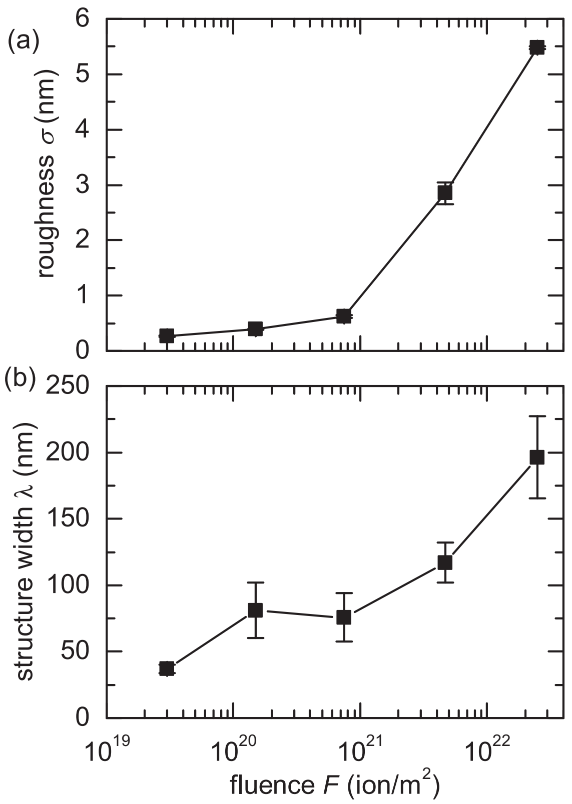

FIG. 5. Dependence of (a) roughness σ and (b) structure width λ on fluence F for 2 keV Kr$^+$ ion irradiation at $T = 704$ K.

that are bounded by monatomic, single steps. The single steps imply terraces with alternating dimer row directions. At $F = 1.5 \times 10^{20}$ ions/m^2 [Fig. 4(b)], the pyramidal pits and holes dominate the surface morphology. The step edges are parallel to the ⟨110⟩ directions. The structure width increases to $\lambda = 80$ nm. Increasing the fluence to $F = 7.5 \times 10^{20}$ ions/m^2 leads to pyramids with double steps on the slopes [Fig. 4(c)]. The slope angle distribution shows peaks between 6° and 10° in the ⟨110⟩ directions.

At $F = 4.7 \times 10^{21}$ ions/m^2 [Fig. 4(d)], the pyramidal mounds have become short range ordered with the edges of the pyramid bases oriented along the ⟨110⟩ directions. Neighboring mounds are connected by short ridges running 30°–50° to the ⟨110⟩ directions. In addition to the peaks between 6° and 8°, slope angles up to 25° in the ⟨110⟩ directions are present (see also Sec. III).

At the highest fluence investigated, $F = 2.5 \times 10^{22}$ ions/m^2 [Fig. 4(e)], the surface exhibits a network of ridges and valleys now running approximately (deviations up to 15°) in the ⟨100⟩ rather than the ⟨110⟩ directions, that were predominant at lower fluences. Though Fig. 4(e) appears to display a slight preference for ridges close to the horizontal direction, by analysis of many topographs it was firmly established that their distribution obeys a fourfold symmetry. The step edges of the ridges are kinked with straight parts still in the ⟨110⟩ directions with a length of 10 nm to a few tens nm. On top of the ridges, there are pyramidal mounds with the bases oriented along the ⟨110⟩ directions, which can be seen in the 360 nm × 360 nm size, second row, image of Fig. 4(e). The height difference between the valley and the ridges is ≈25 nm. The slopes of the ridges consist mostly of step bunches, while the pyramids on top of the ridges also have double steps separated by ≈2-nm-wide terraces. The roughness of the surface here is $\sigma = 5.5$ nm.

V. DISCUSSION

From previous work it is known that under low energy ion beam erosion the selvage of a semiconductor surface becomes amorphized below a critical temperature, while it remains crystalline above T_c. Examples are 1 keV Ar$^+$ on Si(001) [30] ($T_c = 400\,^\circ$C–$500\,^\circ$C), 240 eV Xe$^+$ on Ge(001) [29] ($T_c = 165\,^\circ$C), and also B, P, and Sb implantation into Si [36]. It is striking in our experiments to see how sharp this transition takes place. After erosion at 664 K in Fig. 1(a) the sample is entirely amorphous in LEED and STM, while with a temperature increase to 674 K, just by 10 K, LEED displays a clear crystalline diffraction pattern with a (2 × 1) dimer row reconstruction and STM a well developed step and terrace structure. The sharpness of this transition can also be inferred from an additional experiment without ion beam exposure at elevated temperature. After room temperature irradiation, the amorphous selvage remains amorphous even after extended annealing for 1800 s at 664 K, as apparent from the LEED pattern in Fig. 6(a), while annealing an identically prepared sample for the same time just to a temperature being 10 K higher results in a clear, well developed crystalline LEED pattern with a (2 × 1) dimer row reconstruction as shown in Fig. 6(b).

While with our current tools we are unable to obtain insight into the dynamics of the amorphous/crystalline phase transition, we are convinced that it would be rewarding to study this phase transition around $T_c = 670$ K in a microscopic experiment with time resolution and precise temperature control as it could, for instance, be realized in a low energy electron microscope.

For the low fluxes used here, we find the transition not to depend on ion flux down to the limit of zero flux (compare Fig. 6). It seems that the transition temperature is insensitive to the details of the experiment. That is, above T_c the amorphous pockets created through ion impacts in Si(001) are entirely

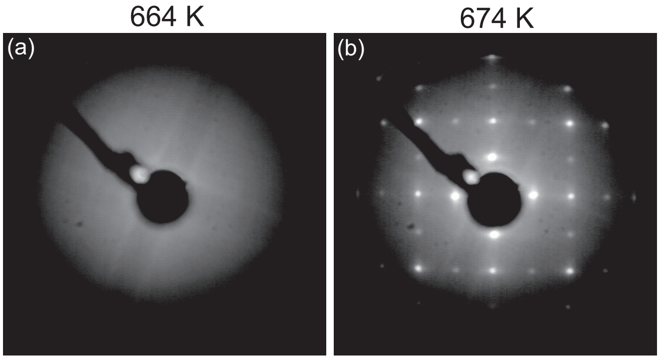

FIG. 6. LEED patterns at 66 eV electron energy after annealing of ion beam amorphized Si(001) for 1800 s to (a) 664 K and (b) 674 K.

crystallized well before a subsequent impact within the same location takes place.

Our findings on the sharpness and insensitivity of the amorphous to crystalline transition for Si(001) are not entirely in agreement with previous work: Ozaydin *et al.* [30] found with 1 keV Ar^+ irradiation an extended transition temperature range between 670 and 770 K, inconsistent with the sharpness of the transition observed by us. Using 500 eV Xe^+ Ou *et al.* [32] find a temperature range of pattern formation for Si(001) between 750 and 850 K, while we observe the most pronounced and roughest patterns already at 700 K. The reasons for these discrepancies are unclear, but we emphasize that the experiments described here were conducted under ultrahigh vacuum conditions and for samples without native oxide. Since surface diffusion processes are of decisive relevance for pattern formation processes, one might speculate that the surface condition and cleanness *during* ion erosion might be of great relevance for the pattern formation.

Also compared to other metallic and semiconducting materials, the range of pattern formation on Si(001) found by us is remarkably narrow extending from about $T_c = 670$ K to 720 K. For comparison, for Ge(001) it is from 530 to 700 K [31], for Ag(001) from 200 to 440 K, for Ag(110) from 180 to 340 K [11], for Pt(111) from 200 to 700 K [10]. The broader temperature range for metals is straightforward to understand, since metals remain crystalline during ion erosion and together with the onset of surface diffusion pattern formation sets in [10].

This narrow temperature range of roughening is associated to the sharply peaked roughness maximum around $T \approx 700$ K, which is located only 30 K above the transition from amorphous to crystalline Si and with σ about an order of magnitude larger than outside the temperature range of roughening. Towards lower temperatures, roughness buildup is limited eventually by amorphization. The crystalline anisotropy, anisotropic material transport, diffusion, and the kinetic barriers decisive for roughness buildup can only be relevant, if the crystalline structure is maintained with sufficient perfection, i.e., without too many defects. Towards higher temperatures, roughness buildup is limited by more and more efficient diffusion, resulting in increasing length scales and turning kinetic barriers irrelevant. In the following we discuss the origin of the roughness buildup through the formation of pits and mounds in more detail.

On samples that remain crystalline during ion erosion, surface vacancies and adatoms (or small clusters of these species) are the mobile, diffusing species crucial for surface morphological evolution. (If mobile, bulk vacancies and interstitials will rapidly turn into surface vacancies and adatoms; if not, the receding surface will do so.) Usually, adatoms efficiently recombine with surface vacancies. Then only surface vacancies are left that reflect sputtering. Mobile surface vacancies migrate, nucleate into immobile vacancy clusters, and subsequently grow by incorporation of additional surface vacancies [7–9,31]. To understand whether a surface remains smooth or not, the fate of vacancies created within an existing vacancy island is of crucial importance [8,26,27,37]: If their annealing to ascending steps is kinetically hindered, new vacancy islands form at the bottom of existing ones prior to coalescence of the existing ones. Consequently, pit formation is initiated. The situation corresponds to the one during epitaxial growth, where an additional barrier for annealing of the deposited atoms to descending steps [the Ehrlich-Schwoebel (ES) barrier [38,39]] implies nucleation of adatom islands on top of existing ones prior to their coalescence, and thus mound formation [40]. In the continuum description of epitaxial growth, neglecting nucleation, the effect of the ES barrier is an uphill current [41] giving rise to a growth instability. A step edge barrier for vacancies (a vacancy ES barrier) also gives rises to an effective uphill mass current and thus to an instability during erosion. Note that the arguments still hold even if recombination of adatoms and surface vacancies is hampered [37], since both defect species separately give rise to uphill mass currents, i.e., their destabilizing effects add rather than cancel. While this picture is adequate for small slopes (low step concentrations), Siegert and Plischke [42] pointed out that at some slope the surface currents *must* vanish and kinetic facets are selected, irrespective of the precise origin of the cancellation. During ion erosion the ballistic mass drift due to the ion beam [43] is likely to contribute significantly to the cancellation of surface currents. On Si(001) this general picture has to be complemented by the fact that the (2×1) dimer row reconstruction induces anisotropic diffusion—e.g., the vacancy diffusion along the dimer rows is much faster than perpendicular to them [44]—which contributes to the pattern anisotropy. Also, step edges parallel to the $\langle 110 \rangle$ directions are energetically favored [34,45]. As diffusion along the steps is faster than across the dimer rows [46], step diffusion contributes significantly to the formation of the pyramidal shape by straightening the steps.

To obtain deep pits, two factors are important: (i) a sparse nucleation of the initial vacancy islands (because of slope selection), and (ii) a maximum slope within the pits (an effective vacancy ES barrier). Beyond T_c, the mobility of vacancies will increase with temperature and the nucleation density will decrease, favoring roughness buildup. Therefore, to explain the dramatic decay of the roughness in the limited temperature interval from 700 to 720 K, one needs to invoke a process that is relevant on the time scale of the experiment, changes its frequency substantially in this narrow temperature interval, and that affects the efficiency of the vacancy ES barrier. The relevant time scale of the experiments is seconds, as with the fluxes used in the experiments a substantial fraction of an atomic Si layer (of the order of 10%) is removed within a second. Assuming an Arrhenius-type behavior for this activated process with a usual attempt frequency $\nu_0 \approx 10^{13}$ s^{-1} one estimates an activation barrier for a relevant process (frequency $\nu \approx 1$ s^{-1}) of about 1.8 eV. A process with a significantly larger activation barrier will not take place on the experimental time scale, while a process with a much smaller activation energy will always proceed at the experimental time scale, be the temperature 700 or 720 K. A relevant process with an activation energy of $\approx$1.8 eV changes its frequency by about a factor of 2.3 between 700 and 720 K. Such a process that affects the efficiency of the vacancy ES barrier could be the onset of vacancy annealing right at ascending steps as suggested by Ou *et al.* [31]. Alternatively, the onset of atom detachment from steps and the formation of an adatom lattice gas, which then effectively anneals vacancies irrespective of their precise location, could have the same effect. The latter mechanism was demonstrated to drive the transition form pit formation to layer-by-layer removal in ion erosion of Pt(111) [8,47]. Further experiments and calculations are certainly necessary to pinpoint the decisive atomic process.

Assuming the structure width λ of the morphology to be determined by the initial length scale λ_i set by vacancy nucleation, one expects a dependence $\lambda \propto \Phi^{-\chi}$ of the length scale on the ion flux Φ (Ref. [48]), where χ is a scaling exponent. However, Fig. 5(b) does not display such a flux dependence for the two data sets with fluxes differing by a factor of 3. A number of reasons may be responsible for the absence this variation: (i) The scaling exponent χ may be as small as 1/6 for a critical nucleus of size 1 which would result in a length scale ratio of 1.2, well within the limits of our experimental uncertainties. (ii) Due to the complexity of the single ion damage and the width of its damage distribution, the nucleation might have a weaker dependence on ion flux as expected, or even none. (iii) Slope selection and coarsening might equalize differences in the initial length scale λ_i after the large ion fluences, for which λ is evaluated.

Next, we will discuss the change of the surface morphology with increasing ion fluence from a surface with pyramidal mounds and pits oriented along the $\langle 110\rangle$ directions [compare Fig. 4(d)] to ridges and valleys approximately oriented parallel to the $\langle 100\rangle$ directions [compare Fig. 4(e)]. This change coincides with a coarsening of the pattern [compare Fig. 5(b)]. Figure 7 sketches a model capable of explaining this pattern rotation and its relation to coarsening. During coarsening neighboring pyramids will touch at their corners and share steps with inward (concave) and outward (convex) 90° corners. The slopes of pyramids are composed of narrow $\approx$2–4 nm terraces with the dimer rows perpendicular to the double steps. Surface vacancies and adatoms created on the terrace will eventually become step adatoms and step vacancies, irrespective whether they arrive to the step from the descending or ascending side [Fig. 7(a)]. Step vacancies and step adatoms diffuse along the step edge until they are incorporated into a kink site. This step-edge diffusion is much faster than terrace diffusion perpendicular to the dimer rows [46]. Incorporation at kink sites is asymmetric for concave and convex kinks [see Fig. 7(a)]. Step vacancies are preferentially incorporated into convex kinks (B) and adatoms into concave kinks (A), whereby each species contributes to a reduction of the number of broken bonds. Thereby the incorporation of vacancies and adatoms into a step with 90° corners leads to their smoothing until an orientation intermediate between the initial 90° step segments is reached. In the thermodynamic language, the high chemical potential at convex corners and the low one at concave corners leads to a smoothening of the step. This process takes place even in the absence of thermal fluctuations, as long as the arriving mobile species remain mobile along the step. Due to randomness in the initial positioning, some neighboring pyramids will touch during erosion, others not, as shown in Fig. 7(b). The resulting transport along the edges of pyramids that touch, as indicated by arrows in Fig. 7(b), leads to the formation of ridges between some of the pyramids [compare Fig. 7(c) and Fig. 4(d)], and in the long term these ridges will be rotated approximately 45° with respect to the edge of the original pyramids resulting in a pattern as in Fig. 4(e). The height of a ridge from the bottom of the valley to the top is >14 nm, which corresponds to $\approx$100 monolayers. Figure 4(d) shows that the pyramids are connected with multiple neighboring pyramids by small ridges already at $F = 4.7 \times 10^{21}$ ions/m^2. The broader distribution of ridge directions can be understood by taking into account that the surface at 4.7×10^{20} ions/m^2 is only short range ordered. This broad distribution of directions between neighboring pyramids leads to the spread in ridge directions in Fig. 4(e). We note that only the initial disorder enables coarsening and the formation of the rotated ridge segments. If the pyramids would be arranged in a perfectly ordered checkerboard pattern, they would connect to all four neighbors, no convex kinks would be present, and no coarsening would take place. The pyramids on top of the ridges at $F = 2.5 \times 10^{22}$ ions/m^2 [Fig. 4(e)] are remainders of the pyramids at lower fluences. As they are higher than the ridges, there is no step edge running to a second pyramid, so the mechanism discussed above is not operative and the edges of the pyramids stay parallel to the $\langle 110\rangle$ directions.

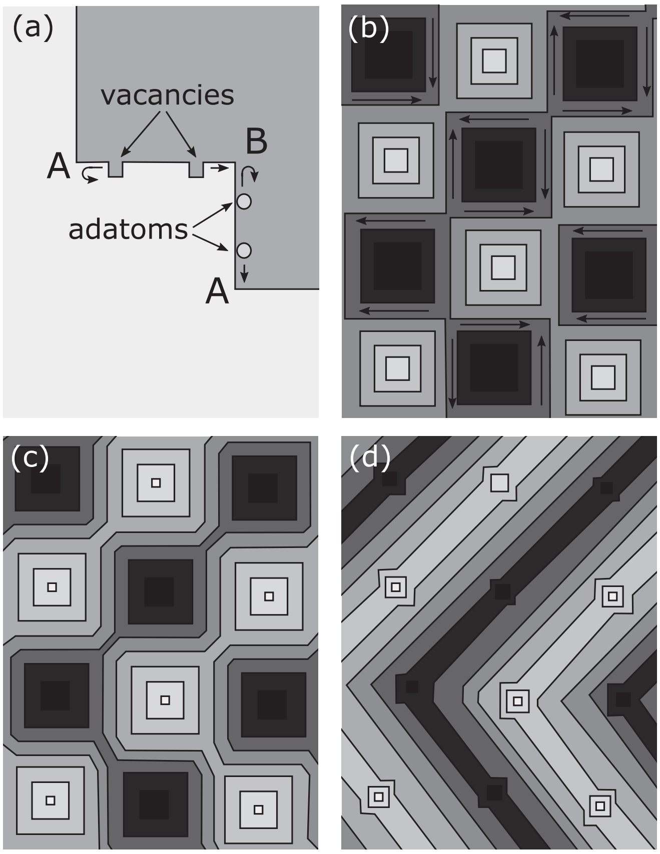

FIG. 7. (a) Asymmetric incorporation of vacancies and adatoms diffusing along step edges at kink sites; two terraces separated by a step are shown. The lower terrace is shaded darker and the upper lighter. (b)–(d) Our model of pattern rotation (see text). The shading indicates the height from dark (low) to light (high).

To the authors' best knowledge, for *normal ion incidence* erosion, a rotation of a surface pattern as a function of *ion fluence* has not been reported before. However, for *grazing incidence* ($\approx$ 60°) transitions from ripples oriented perpendicular to the ion beam to ripples parallel to the ion beam have been observed on Si(111) [49] and Si(001) [17,50] as functions of the fluence. These ripple rotations were rationalized by a saturation of the ripple mode perpendicular to the ion beam and continuing growth of the ripple mode parallel to the ion beam. In contrast, our explanation for the pattern rotation at normal incidence leaves the framework of continuum theory and pinpoints the atomistic process—step-edge diffusion—and makes the close connection of pattern rotation and coarsening obvious. Finally, it should be mentioned that for *normal ion incidence* ion erosion of metal substrates ion beam pattern rotations have been reported as a function of *temperature* [11,12] being linked to the hierarchy of surface diffusion processes and their temperature dependent time scales.

It is also interesting to compare our results to the findings of Ou *et al.* [31,32] for the (001) surfaces of Ge and Si. For Ge the authors find the pit edges parallel to ⟨001⟩, while for Si the authors observe edges parallel to ⟨110⟩. Since no fluence dependence is reported for Si and Ge in Ref. [32] and the lowest fluence 1×10^{21} ions/m^2 in Ref. [31] is already rather high, this surprising difference may reflect just snapshots of a universal behavior, where pits change their edge orientation from ⟨001⟩ to ⟨110⟩ with increasing fluence.

VI. CONCLUSION

Low energy ion beam pattern formation on Si(001) near the critical crystallization temperature $T_c = 670$ K was investigated as a function of temperature and ion fluence. In a narrow temperature range from T_c to 720 K the surface roughens by more than an order of magnitude and a pit and mound morphology develops. The roughness peaks around $\approx$700 K and rapidly diminishes towards higher temperatures. The slopes of the pits are composed of small terraces carrying Si-dimer rows, which are separated by double steps along ⟨110⟩, and in the steepest parts by bunches of such steps. Pattern formation in this temperature range is driven by a diffusional instability due to the surface vacancy Ehrlich-Schwoebel barrier. Its effect vanishes below T_c due to the lack of crystallinity and fades away at higher temperatures most likely through a mechanism efficiently bypassing the vacancy ES barrier, e.g., the formation of an adatom lattice gas.

At around 700 K a fluence dependent pattern rotation is found, which was not anticipated before: While for low fluences the pits and mounds are aligned with the ⟨110⟩ directions, as expected form the atomic step structure, for large fluences a ridge and valley pattern forms that is aligned with ⟨001⟩ directions. It is shown that the pattern rotation is intimately linked to the coarsening of the pattern and results from step-edge diffusion induced smoothing in consequence of coalescence of neighboring pyramids.

ACKNOWLEDGMENTS

Financial support by Deutsche Forschungsgemeinschaft (DFG) through Research Unit FOR 845 within project DFG MI 581/16-2 and experimental help by Moritz Will are acknowledged.

---

[1] W. L. Chan and E. Chason, J. Appl. Phys. **101**, 121301 (2007).
[2] J. Muñoz-García, L. Vázquez, M. Castro, R. Gago, A. Redondo-Cubero, A. Moreno-Barrado, and R. Cuerno, Mater. Sci. Eng., R **86**, 1 (2014).
[3] M. Ranjan, S. Facsko, M. Fritzsche, and S. Mukherjee, Microelectron. Eng. **102**, 44 (2013).
[4] B. Teshome, S. Facsko, and A. Keller, Nanoscale **6**, 1790 (2014).
[5] C. Martella, D. Chiappe, C. Mennucci, and F. B. de Mongeot, J. Appl. Phys. **115**, 194308 (2014).
[6] T. Basu, M. Kumar, A. Kanjilal, J. Ghatak, P. K. Sahoo, and T. Som, J. Appl. Phys. **116**, 114309 (2014).
[7] T. Michely and G. Comsa, Surf. Sci. **256**, 217 (1991).
[8] T. Michely, M. Kalff, G. Comsa, M. Strobel, and K.-H. Heinig, Phys. Rev. Lett. **86**, 2589 (2001).
[9] M. Kalff, G. Comsa, and T. Michely, Surf. Sci. **486**, 103 (2001).
[10] H. Hansen, A. Redinger, S. Messlinger, G. Stoian, Y. Rosandi, H. M. Urbassek, U. Linke, and T. Michely, Phys. Rev. B **73**, 235414 (2006).
[11] G. Costantini, S. Rusponi, F. B. de Mongeot, C. Boragno, and U. Valbusa, J. Phys.: Condens. Matter **13**, 5875 (2001).
[12] P. Broekmann, A. Mewe, H. Wormeester, and B. Poelsema, Phys. Rev. Lett. **89**, 146102 (2002).
[13] S. Rusponi, G. Costantini, C. Boragno, and U. Valbusa, Phys. Rev. Lett. **81**, 4184 (1998).
[14] S. Rusponi, G. Costantini, C. Boragno, and U. Valbusa, Phys. Rev. Lett. **81**, 2735 (1998).
[15] S. Macko, F. Frost, B. Ziberi, D. F. Förster, and T. Michely, Nanotechnology **21**, 085301 (2010).
[16] S. Macko, F. Frost, M. Engler, D. Hirsch, T. Höche, J. Grenzer, and T. Michely, New J. Phys. **13**, 073017 (2011).
[17] M. Engler, F. Frost, S. Müller, S. Macko, M. Will, R. Feder, D. Spemann, R. Hübner, S. Facsko, and T. Michely, Nanotechnology **25**, 115303 (2014).
[18] M. Engler, S. Macko, F. Frost, and T. Michely, Phys. Rev. B **89**, 245412 (2014).
[19] M. Teichmann, J. Lorbeer, B. Ziberi, F. Frost, and B. Rauschenbach, New J. Phys. **15**, 103029 (2013).
[20] A. Moreno-Barrado, M. Castro, R. Gago, L. Vázquez, J. Muñoz-García, A. Redondo-Cubero, B. Galiana, C. Ballesteros, and R. Cuerno, Phys. Rev. B **91**, 155303 (2015).
[21] S. Facsko, T. Dekorsy, C. Koerdt, C. Trappe, H. Kurz, A. Vogt, and H. L. Hartnagel, Science **285**, 1551 (1999).
[22] G. Ozaydin-Ince and K. F. Ludwig, Jr., J. Phys.: Condens. Matter **21**, 224008 (2009).
[23] T. Basu, D. Datta, and T. Som, Nanoscale Res. Lett. **8**, 289 (2013).
[24] K. Zhang, H. Hofsäss, F. Rotter, M. Uhrmacher, C. Ronning, and J. Krauser, Surf. Coat. Technol. **203**, 2395 (2009).
[25] M. Teichmann, J. Lorbeer, F. Frost, and B. Rauschenbach, Nanoscale Res. Lett. **9**, 1 (2014).
[26] D. Cherns, Philos. Mag. **36**, 1429 (1977).
[27] B. Poelsema, R. Kunkel, L. K. Verheij, and G. Comsa, Phys. Rev. B **41**, 11609 (1990).

[28] H. Hofsäss and R. M. Bradley, J. Appl. Phys. **117**, 174310 (2015).
[29] S. J. Chey, J. E. Van Nostrand, and D. G. Cahill, Phys. Rev. B **52**, 16696 (1995).
[30] G. Ozaydin, J. Karl F. Ludwig, H. Zhou, L. Zhou, and R. L. Headrick, J. Appl. Phys. **103**, 033512 (2008).
[31] X. Ou, A. Keller, M. Helm, J. Fassbender, and S. Facsko, Phys. Rev. Lett. **111**, 016101 (2013).
[32] X. Ou, K.-H. Heinig, R. Hübner, J. Grenzer, X. Wang, M. Helm, J. Fassbender, and S. Facsko, Nanoscale **7**, 18928 (2015).
[33] D. Nečas and P. Klapetek, Open Phys. **10**, 181 (2011).
[34] M. Hanbücken, B. Röttger, and H. Neddermeyer, Surf. Sci. **331–333**, 1028 (1995).
[35] M. Webb, Surf. Sci. **299–300**, 454 (1994).
[36] L. Pelaz, L. A. Marqués, and J. Barbolla, J. Appl. Phys. **96**, 5947 (2004).
[37] T. Michely and G. Comsa, Phys. Rev. B **44**, 8411 (1991).
[38] G. Ehrlich and F. G. Hudda, J. Chem. Phys. **44**, 1039 (1966).
[39] R. L. Schwoebel and E. J. Shipsey, J. Appl. Phys. **37**, 3682 (1966).
[40] J. Krug, P. Politi, and T. Michely, Phys. Rev. B **61**, 14037 (2000).
[41] J. Villain, J. Phys. I (France) **1**, 19 (1991).
[42] M. Siegert and M. Plischke, Phys. Rev. Lett. **73**, 1517 (1994).
[43] G. Carter and V. Vishnyakov, Phys. Rev. B **54**, 17647 (1996).
[44] N. Kitamura, M. G. Lagally, and M. B. Webb, Phys. Rev. Lett. **71**, 2082 (1993).
[45] H. J. W. Zandvliet, O. Gurlu, R. van Gastel, and B. Poelsema, Phys. Rev. B **69**, 125311 (2004).
[46] C. Roland and G. H. Gilmer, Phys. Rev. B **46**, 13437 (1992).
[47] T. Michely, T. Land, U. Littmark, and G. Comsa, Surf. Sci. **272**, 204 (1992).
[48] T. Michely and J. Krug, *Islands, Mounds and Atoms*, Springer Series in Surface Sciences Vol. 42 (Springer, Berlin, 2004).
[49] A.-D. Brown, J. Erlebacher, W.-L. Chan, and E. Chason, Phys. Rev. Lett. **95**, 056101 (2005).
[50] A. Keller, S. Roßbach, S. Facsko, and W. Möller, Nanotechnology **19**, 135303 (2008).